The International Journal of Advanced Manufacturing Technology (2024) 135:763–774
https://doi.org/10.1007/s00170-024-14582-9

ORIGINAL ARTICLE

Additive friction stir deposition of al 7075 parts and the effect of heat treatment on microstructure, electroconductivity, and mechanical properties

Ehsan Bagheri[1] · **Saeid Zavari**[1] · **Noushin Adibi**[1] · **Huan Ding**[1] · **Hamed Ghadimi**[1] · **Shengmin Guo**[1]

Received: 3 June 2024 / Accepted: 23 September 2024 / Published online: 2 October 2024

Abstract

Additive friction stir deposition (AFSD) is a relatively new metal additive manufacturing technique with many advantages compared to fusion-based methods. Despite the recent developments, the research about AFSD is in the initial stages, and processing hard and strong materials such as Aluminum 7075 is still challenging. In this study, a set of processing parameters is introduced and optimized for the AFSD of defect-free Al 7075 parts. Microstructure, electroconductivity, and mechanical properties of the as-deposited parts are studied. Compared with feedstock, the results indicated that the conductivity of the printed specimens increased by 19.5%, and the strength and hardness experienced a significant decrease by 54.4% and 43.5%, respectively. The change in the properties was associated with the precipitation enlargement and aggregation during the AFSD process. Subsequently, heat treatment was conducted to recover the mechanical properties, and noteworthy enhancements, a 101.2% increase in hardness and a 49.1% increase in strength, were recorded compared to the as-deposited condition due to the smaller and more uniformly distributed secondary phases in the matrix.

Keywords Additive friction stir deposition · Aluminum alloy · Microstructure · Mechanical properties

1 Introduction

Metal additive manufacturing (AM) is a disruptive technology that has provided great opportunities for various industries due to its numerous advantages. Some of these benefits are enhanced design freedom, reduced production lead time and wastes, custom fabrication, and rapid prototyping. Fusion-based metal additive manufacturing has been introduced as one of the first commercial techniques, and it is still dominating the market today [1, 2]. However, some of the inherent constraints related to the fusion-based AM technique have caused a gap between the production capabilities and industrial demands. Solidification-related defects such as porosity, residual stress, distortion, hot cracking, elemental segregation, and elemental loss are examples of such constraints that deteriorate the quality of the parts prepared by fusion-based methods [3]. Therefore, it is vital to develop AM techniques that process metallic alloys in the solid state rather than melting them and subsequent solidification to prevent the aforementioned issues.

Friction-based additive manufacturing is a plasticity-based solid-state process that has emerged as a promising alternative to fusion-based 3D printing methods. It involves severe shear deformation of the material induced by the frictional forces to build the desired shape layer-by-layer. Friction extrusion additive manufacturing, hybrid metal extrusion and bonding, and additive friction stir deposition (AFSD) are three common friction-based additive manufacturing methods [4]. AFSD, commercially named MELD, is the most prevalent solid-state AM technique which renders considerable advantages regarding production efficiency, flexibility, and cost. The process involves feeding the feedstock rod to a substrate surface through a hollow rotating tool. The tip of the feedstock rod is softened due to the heat generated by frictional forces and deposited onto the substrate due to the traverse motion of the tool. Material feed rate (F), tool rotational speed (ω), layer thickness (T), and tool traverse velocity (V) are the major parameters in the AFSD process which control the deposition quality. The higher the rotational speed and the lower the traverse

---

✉ Shengmin Guo
sguo2@lsu.edu

[1] Department of Mechanical and Industrial Engineering, Louisiana State University, Baton Rouge, LA 70803, USA

velocity result in higher heat input, which influences the part's quality and properties significantly [5, 6]. Common surface defects observed in AFSD are excessive material flash, onion ring pattern, galling, surface scratch, and edge cracking which can be removed by adjusting the processing parameters [7]. Therefore, optimization of the parameters is essential to acquire a defect-free deposition with the best possible properties.

AFSD has been successfully employed for the deposition of different Al alloys including softer series of 5xxx and 6xxx and harder series such as 2xxx and 7xxx. Several studies have been performed to find out the relations between the processing parameters and the printed part's properties [4, 8–25]. For instance, Philips et al. [22] reported successful deposition of Al 5083 by AFSD and investigated the mechanical properties and microstructure of the as-deposited part. Ghadimi et al. [15] worked on AFSD of Al 6061 to study the effect of different deposition parameters on the tensile properties of the fabricated parts. In another study by Ghadimi et al. [14], the hardness distribution and microstructure of the deposited Al 2050 parts were studied. Al 2219 was 3D printed by Rivera et al. [23] to study the tensile and microstructure of the as-deposited parts. Ahmed et al. [8] deposited Al 2011 without any physical discontinuities or interfacial defects between layers in the building direction. Grain refinement is a common phenomenon reported in AFSD studies. It is due to dynamic recrystallization caused by the high temperature (above half of the melting temperature) and large plastic deformation in the process [7]. Furthermore, in many studies on AFSD of Al, the hardness, strength, and corrosion resistance of the as-deposited part are found to be worsen compared to the feedstock material. The reason for these decreases is ascribed to the change in the strengthening mechanism and loss of hardening precipitations after AFSD [6]. This indicates the importance of heat treatment after AFSD to recover the properties. The as-fabricated Al 6061 parts were subjected to T6 heat treatment by Zeng et al. [24], and the hardness for the heat-treated parts is comparable to that of the feedstock. Moreover, Chen et al. [11] investigated the effect of heat treatment on Al 6061 samples prepared by AFSD and found that the strength was increased by 18%.

The 7xxx series of Al alloys have been extensively utilized in the aerospace industry and military sectors due to their high specific strength, good fatigue properties, and machinability. Considering the challenges associated with fusion-based additive manufacturing of Al 7xxx due to its non-weldable nature, it is vital to develop solid-state techniques such as AFSD [20, 26] for processing Al 7xxx. There are several studies on one-layer deposition of 7xxx series of Al alloys, specifically Al 7075, for repairing purposes [27, 28]. However, the number of papers on AFSD of multilayers is much less than the other alloys. The higher hardness and strength of Al 7075 make the AFSD process more challenging. Avery et al. [9] deposited an Al 7075 block with a feedstock feed rate and traverse velocity of 50.8 mm/min and rotational speed of 250 rpm. The microstructure and mechanical properties of the deposition were assessed. The results revealed a refined microstructure for the deposition. Hardness, tensile strength, and fatigue life of the printed block were lower than the feedstock material. The effect of heat treatment on the properties of the deposition was not studied. In addition, excessive flash was observed in the printed block which was due to improper selection of processing parameters. Cahalan et al. [10] explored the influence of overlapping parallel pass depositions by AFSD on the mechanical properties of Al 7075. Feedstock feed rate, traverse velocity, and rotational speed were 69.9 mm/min, 127 mm/min, and 275 rpm, respectively. They indicated that components with comparable properties to single-row depositions could be obtained by adjusting the overlapping deposition paths. Elshaghoul et al. [13] studied the feasibility of 3D printing Al 7075 on an Al 2024 substrate by AFSD and optimization of the deposition parameters. The parts were fabricated by pushing a rotating Al 7075 feeding rod 4 cm in diameter onto the Al 2024 substrate without moving in the traverse direction. Physically defect-free depositions were successfully obtained using a rotational speed of 400 rpm and material feed rates of 1, 2, 3, and 4 mm/min.

In the present work, detailed processing parameters are introduced and optimized for the AFSD of defect-free Al 7075 parts. Since a fast deposition rate is more desirable for industry, effort is made to introduce higher deposition parameters in this study compared to the literature. Next, two Al 7075 blocks are deposited using the optimized parameters and one of them is subjected to heat treatment. Microstructural, mechanical, and electrical conductivity tests are performed on the two parts to determine the performance of the as-deposited material at different layers and find out if the heat treatment can recover the performance of the part. This study provides the groundwork for the implementation of AFSD for the fabrication of Al 7075 parts for engineering applications.

2 Materials and method

Al 7075 square rods with dimensions of 9.5 × 9.5 × 457.2 mm^3 were cut from Al 7075-T651 plates (OnlineMetals) using a waterjet cutter and utilized as the feedstock material. A MELD L3 machine equipped with a H13 tool was employed for 3D printing. This tool has two pairs of teardrop-shaped protrusions around 2.3 mm in height. The protrusions were located on the bottom surface of the tool in a centrosymmetric array, two of them surrounding the feedstock rod outlet and the other pair near the edge of the tool. They assist in material flow and heat generation due to an increase in frictional forces. In addition, they can re-stir the previously deposited layer depending on the layer thickness selection.

An Al 7075-T651 plate (*L*: 304.8 × *W*: 101.6 × *T*: 12.7 mm^3) was employed as the substrate to 3D print the material on it. A thermocouple was placed below the substrate to provide an estimate of the processing temperature. The substrate was heated to 250 °C prior to the deposition to assist in printing the first layers. The feedstock rods were coated with a thin layer of graphite as a dry lubricant prior to being fed to the machine to prevent them from jamming inside the tool during the AFSD. Schematics of the process and the deposition tool are shown in Fig. 1a and b, respectively. The process started by pushing down the rods against the substrate to generate enough heat for material flow, and the parts were deposited layer-by-layer based on a G-code. The relation between the processing parameters is given by the continuity equation (Eqs. 1 and 2) [29, 30].

$$\dot{m}_{\text{in}} = \dot{m}_{\text{out}} \tag{1}$$

$$a^2\dot{y} = wt\dot{x} \tag{2}$$

where a is the side of the feedstock cross-section, $\dot{y}$ is the feedstock feed rate, w is the deposited layer width, t is the deposited layer thickness, and $\dot{x}$ is the traverse velocity. The range of the processing parameters used in this study is summarized in Table 1. Two large blocks with the same length and height of 165.1 and 40.6 mm were deposited and cut based on the schematic indicated in Fig. 1c and d to obtain tensile specimens in the longitudinal direction (XY plane) and two 3-mm-thick slices (YZ plane). The slices were then cut to acquire three samples from the middle section of the building plane named top (T), middle, (M), and bottom (B). This is done to study the properties at different layers. All the samples from one of the blocks were heat treated to T73 conditions according to AMS2772. Briefly, solution treatment was performed at 470 °C for 2 h, followed by water quenching. Then, aging treatment was conducted at 107 °C for 7 h, followed by 177 °C for 8 h. All the samples except for electron backscatter diffraction (EBSD) and tensile

Table 1 Processing parameters used in this study

Parameter	Value
Feedstock feed rate (mm/min)	138.4
Traverse velocity (mm/min)	138.4–194
Tool rotational speed (rpm)	100–200
Initial substrate temperature (°C)	250
Layer thickness (mm)	1.5

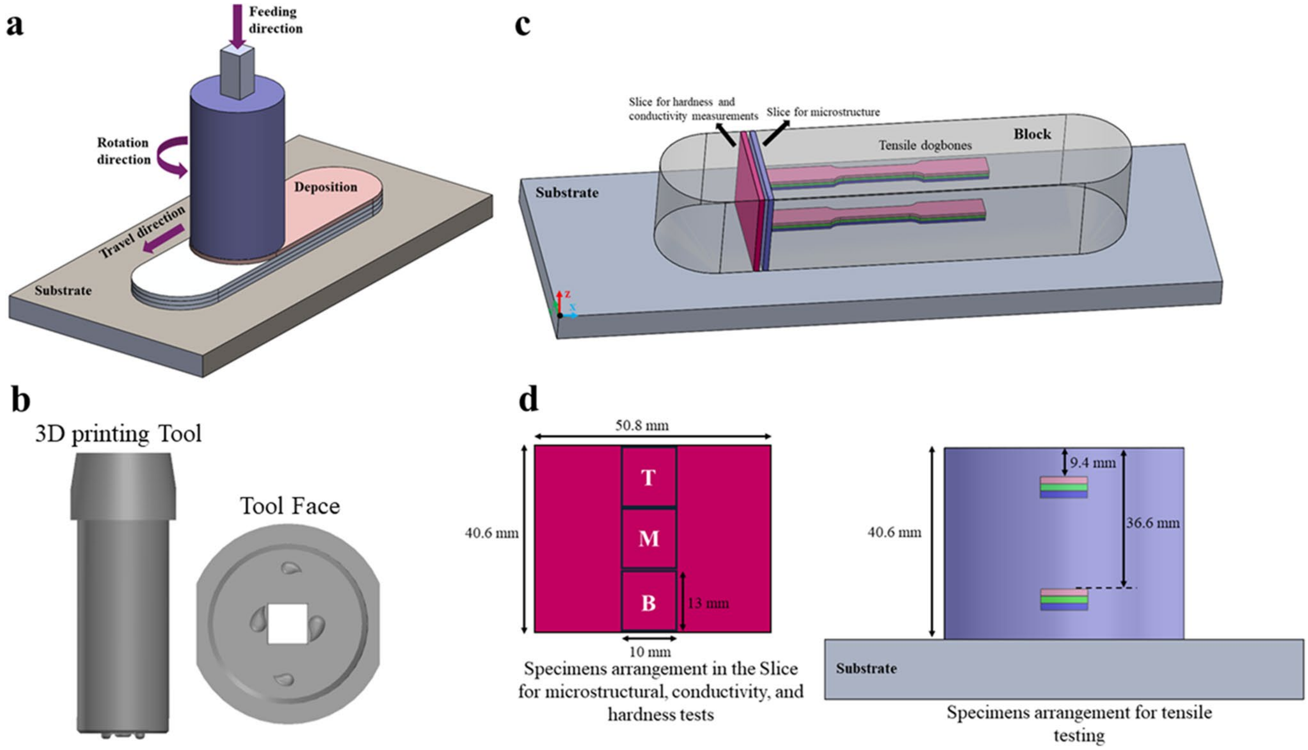

Fig. 1 Schematic of **a** AFSD process, **b** deposition tool, and **c**, **d** specimens cutting design for different characterizations from the deposited blocks

testing ones were polished using SiC papers with different grit sizes (400, 600, 800, 1000, and 1200) and then by polishing pads with polycrystalline diamond suspension (6, 3, and 1 μm) prior to characterization.

The deposited parts were macroscopically inspected to find out the print quality and assess the existence of any common defects in the AFSD such as lack of material and excessive material flash. The machine data recorded during the AFSD were saved and processed to study the processing parameters, downward force, torque, and substrate temperature.

Heat input during the process can be estimated using the torque values recorded by the machine and the processing parameters. It is calculated by Eq. 3 first developed by Pew et al. [31].

$$\text{Heat input} = \frac{2\pi\omega\tau}{60v} \tag{3}$$

where ω is the tool rotational speed in rpm, τ is the torque in N.m, and v is the traverse velocity in m/min.

X-ray diffraction (XRD) analysis was performed to investigate the phase structure of Al 7075 after AFSD and the effect of heat treatment for the top and bottom layer regions. A PANalytical Empyrean diffractometer equipped with PreFIX (pre-aligned, fast, interchangeable X-ray) modules with monochromatic CuKα radiation was employed for this purpose. The patterns were collected from 10 to 90° with a scan step size of 0.01.

A ThermoFisher Helio G5 Xe PFIB/SEM machine was utilized in the backscatter electron (BSE) mode for general inspection of the surface of the cross-section for top and bottom layers before and after the heat treatment. The composition distribution and the grain evolution of the specimens were also studied using the same instrument equipped with energy-dispersive spectroscopy (EDS) and EBSD detectors, respectively. The samples for EBSD were prepared by polishing their surfaces with the PFIB source of the machine.

Microhardness of the different layers was measured along the center line in the building plane before and after the heat treatment using a CM-803 AT microhardness tester. The load and dwell time of the machine were set at 100 gf and 15 s, respectively.

Electroconductivity of the specimens was recorded by a portable instrument (Sigmascope SMP 350, Helmut Fischer GmbH) working based on the eddy current principle. The device was calibrated by standard samples with similar conductivities. The results were presented as percentages according to the International Annealed Copper Standard (%IACS).

Tensile properties of the as-deposited and heat-treated specimens were evaluated based on ASTM E8-E8M. Subsize flat samples were cut from the top and bottom regions in the longitudinal direction (XY plane) as shown in Fig. 1c and d. They were subjected to a tensile rate of 1.2 mm/min using a universal testing machine (TestResources 313) equipped with a 5-kN load cell.

3 Results and discussion

3.1 Macroscopic inspection

The AFSD processing parameters were initially selected based on our prior experiences (138.4 mm/min, 194 mm/min, and 200 rpm for feed rate, traverse velocity, and rotational speed, respectively). Figure 2a shows the surface of

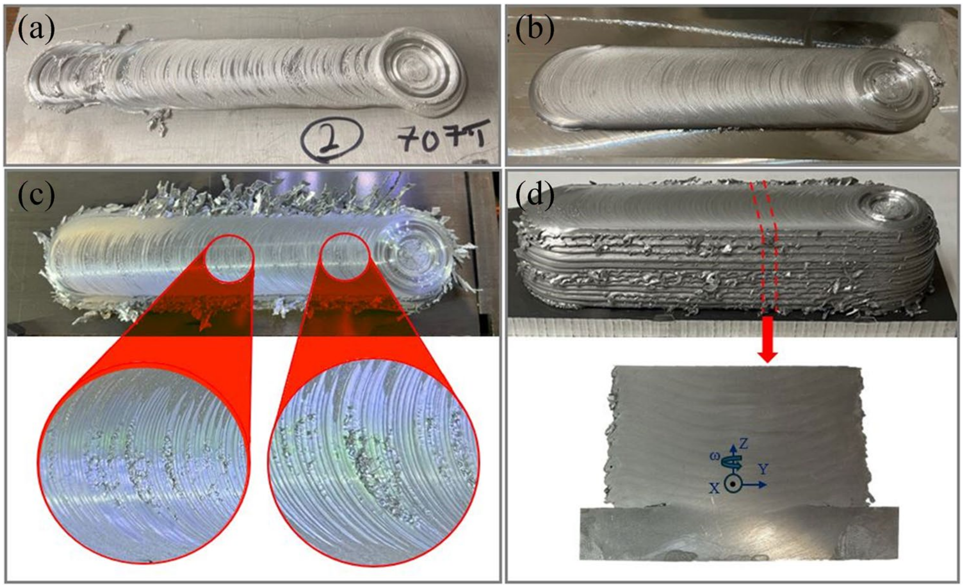

Fig. 2 Photographs of the depositions: **a** the first run at $F = 138.4$ mm/min, $V = 194$ mm/min, and $\omega = 200$ rpm; **b** the first run at $F = 138.4$ mm/min, $V = 138.4$ mm/min, and $\omega = 200$ rpm; **c** multiple layers at $F = 138.4$ mm/min, $V = 138.4$ mm/min, and $\omega = 200$ rpm; and **d** final block at $F = 138.4$ mm/min, $V = 138.4$ mm/min, and $\omega = 150$ rpm

the deposition after the first run based on these conditions. An obvious lack of material can be observed on the surface due to insufficient feeding of the feedstock material. In the next attempt, the traverse velocity was decreased to 138.4 mm/min at the same feed rate and tool rotational speed (194 mm/min, and 200 rpm, respectively) to address this issue. As can be observed in Fig. 2b, the deposited layer was successful with no apparent defects on the surface. However, the surface of depositions was defect-free only for the first couple of layers, and as the process continued, excessive material flash was observed (Fig. 2c). This material flash led to a lack of material on the surface indicated and magnified in two regions by red circles in Fig. 2c.

The reason for the occurrence of the defects after the deposition of subsequent layers stems from the deformation behavior of Al 7075 at elevated temperatures. Undesired surface tearing has been reported in hot extrusion of Al 7075 especially at temperatures above 460 °C. In addition, it has been reported that the tearing can be controlled by reducing the processing temperature [32, 33]. The peak temperature in the AFSD process can be estimated using Eq. 4 [34].

$$\frac{T}{T_m} = K\left(\frac{\omega^2}{v \times 10^4}\right)^a \tag{4}$$

where T_m is the melting temperature of the material; K and α are constants in the ranges of 0.65–0.75 and 0.04–0.05, respectively; and ω is the rotational speed. Based on Eq. 4, the tool rotational speed was decreased from 200 to 150 rpm to reduce the peak temperature. As illustrated in Fig. 2d, the excessive material flash was significantly eliminated after this change in the rotational speed. Therefore, the final block was 3D printed with a feed rate, a traverse velocity of 138.4 mm/min, and a rotational speed of 150 rpm.

For further macroscopic inspection, the polished and etched cross-section of the block is illustrated in Fig. 2d. The layered structure of the part is obvious by the alternating bright and dark regions. This color contrast is attributed to the different crystalline morphology and texture because of the process. The repetitive arrangement of the layers implies the repeatable thermo-mechanical process in AFSD [34]. The structure is different from the commonly observed arrangement due to restirring the layers by the tool protrusions. This restirring distorts the layer boundaries and results in intertwined structures. In addition, all the interfaces between the layers, including the one between the substrate and the first layer, exhibit a curved profile which is also due to the mutual plastic deformation of the layer being deposited and the previous underneath layer.

3.2 AFSD data analysis

The data recorded by the AFSD machine during the deposition of the 26-layer blocks are processed and demonstrated in Fig. 3. The process parameters include downward force, torque, and substrate temperature. The axial downward force

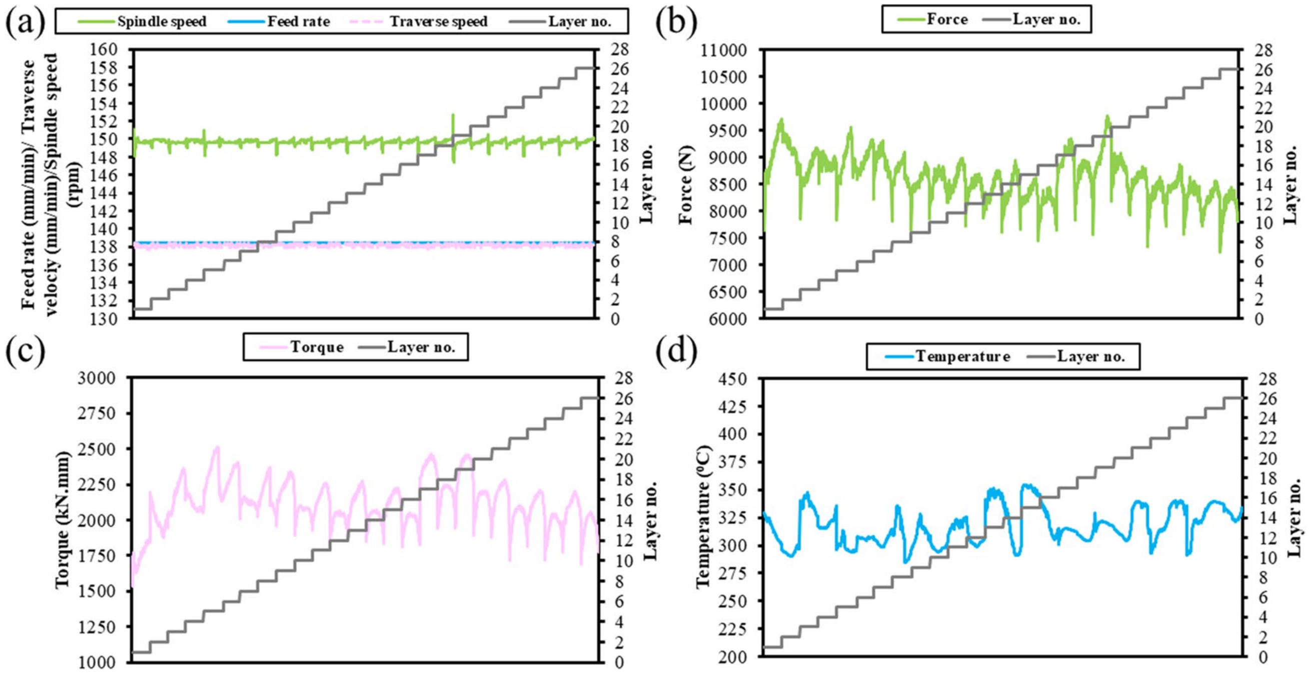

Fig. 3 The processing data recorded by the machine during the deposition of 26 layers: **a** processing parameters, **b** axial force, **c** actuator torque, **d** substrate temperature

(Fig. 3b) is the vertical force applied to the material being deposited. It is required to maintain the force in a certain range during the deposition. It should be high enough to make sure that both sufficient heat and pressure are generated for the material flow and a good bonding between layers. Moreover, the applied force needs to be less than a certain amount depending on the machine design (~ 23 kN for the machine used in this study) to prevent the damage to the machine [15]. The average force recorded for the deposition of the block was approximately 8.6 kN, which met the requirements for a successful deposition. Furthermore, the actuator torque variations are depicted in Fig. 3c. Torque is applied by the tool to the material, and like downward force, it is a critical parameter in AFSD which affects the deposition quality. The average value for torque was 212.2 Nm. It was used to calculate the heat input for the deposition of the block according to Eq. 3, resulting in a value of 24,071.9 J/m. Figure 3d indicates the temperature changes during the process. Although the process started at a substrate temperature of 250 ℃, the actual temperature at which the deposition of the first layer started based on the G-code was around 330 °C. This was due to the initial feeding of the feedstock rod, and pushing it against the substrate would generate extra heat for the plasticization of the material. The average temperature recorded by the thermocouple during the deposition was 317.4 °C. The fluctuation in the temperature diagram indicates the heating/re-heating cycles that the deposition experienced.

3.3 Microstructure investigation

XRD patterns of the feedstock and top and bottom layers of the as-deposited and heat-treated blocks are depicted in Fig. 4. From Fig. 4a, the feedstock exhibited only the peaks attributed to α-Al (FCC) at $2\theta = 38.46$, 44.69, 65.10, 78.12, and 82.13° [35]. However, weak peaks ascribed to η/ή phase ($MgZn_2$) and S phase (Al_2CuMg) were also detected for the as-deposited top and bottom layers. Due to the temperature and pressure provided in the AFSD process, the precipitations, especially metastable ones, dissolved into the Al matrix, reprecipitated, and coarsened based on their thermal cycle history. Hence, the size of the precipitates became larger and detectable by XRD after the process. The formation of larger secondary phases would deteriorate the mechanical properties of the parts which will be investigated in the following sections. Similar XRD results were reported after the AFSD of other Al alloys [14, 24]. The peaks ascribed to the secondary phases almost faded after the heat treatment. During the T73 treatment of the as-deposited parts, the alloying elements first dissolved back into the matrix and finally formed fine and uniformly distributed precipitations after artificial aging.

The diffraction peaks of the feedstock shifted slightly to higher angles after the AFSD as shown in Fig. 4b for $2\theta = 38.46°$. According to Bragg's law, a higher diffraction angle yields a lower interplanar spacing. Therefore, the lattice parameter decreased after the AFSD. This could be due to the formation of large and non-uniform secondary phases [12]. This shift was more prominent for the bottom layers compared to the top specimen because of the different thermal histories for each layer. Compared to the top layers, the bottom ones experienced more heating cycles and maintained a high temperature for a longer time. Hence, the lattice parameter decreased more for the bottom specimen. After the heat treatment, the peaks shifted back to lower angles indicating that the lattice parameter increased due to the formation of fine and uniform precipitation.

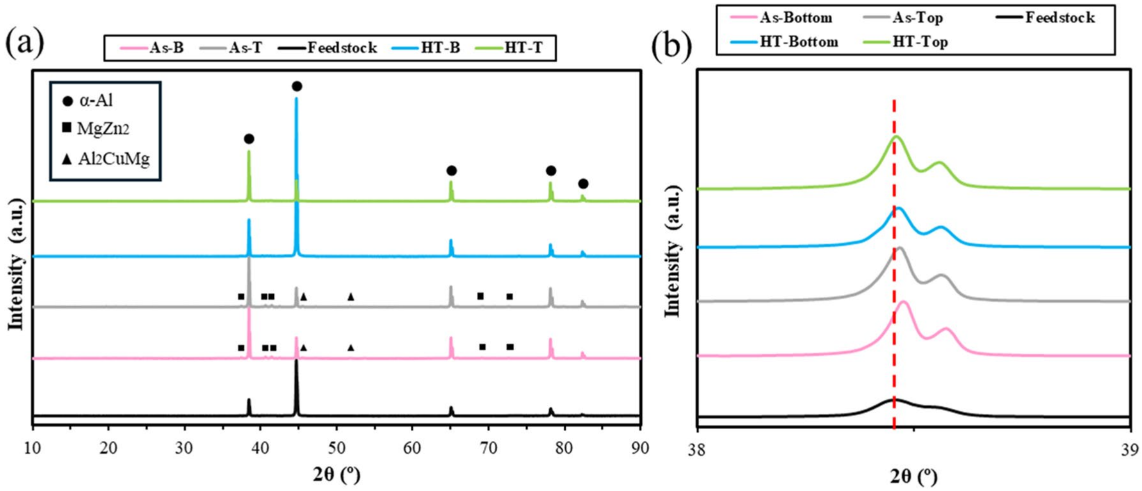

Fig. 4 XRD patterns of the feedstock, as-deposited, and heat-treated specimens

Electron and optical imaging and EDS mapping were utilized to further analyze the secondary phases and composition distribution in the matrix. The results are indicated for the feedstock and the as-deposited specimens in Fig. 5 and for the heat-treated samples in Fig. 6. A smooth surface with almost no apparent particles was observed in the BSE image of the feedstock (Fig. 5a). In addition, uniform distribution of Mg, Zn, and Cu ascribed to the η/ή and S phases was detected for the raw material. However, many large particles appeared on the surface of the as-deposited samples as can be observed in the BSE and optical images (Fig. 5b and c). These particles were attributed to the secondary phases that reprecipitated non-uniformly in the AFSD process [24]. Moreover, the precipitations shown in the BSE image were larger for the bottom layers compared to the top ones. EDS mapping and optical microscopy also confirm the larger size and aggregation of the alloying elements and secondary phases for the bottom layers. This was due to the higher number of heating cycles that the bottom layers experienced during the deposition of the whole block which resulted in precipitation coarsening. After the heat treatment, the number of large secondary phases significantly decreased for both bottom and top specimens. Nevertheless, the bottom layers still contain larger particles compared to the top ones. The results before and after the heat treatment were consistent with the XRD data.

The grain structure of the middle layers before and after heat treatment was studied by EBSD, and the inverse pole figures are depicted in Fig. 7. The as-deposited specimen exhibited a refined equiaxed microstructure with an average grain size of about 4.1 μm (Fig. 7a) compared to the columnar microstructure reported for the feedstock material [36]. The grain refinement during the AFSD was associated with the continuous dynamic recrystallization (CDRX) due to the severe plastic deformation in the process and the high stacking fault energy of Al 7075 [28]. Figure 7b illustrates the obtained grain structure after heat treatment. Compared with the as-deposited EBSD map, the grain size did not experience significant change. This could be attributed to the grain growth impediment by the secondary phases present at the grain boundaries [37]. However, the grains become a little elongated after the treatment. Heat treatment tended to stabilize specific grain orientations. Hence, a more organized texture with less random orientations was acquired after the treatment.

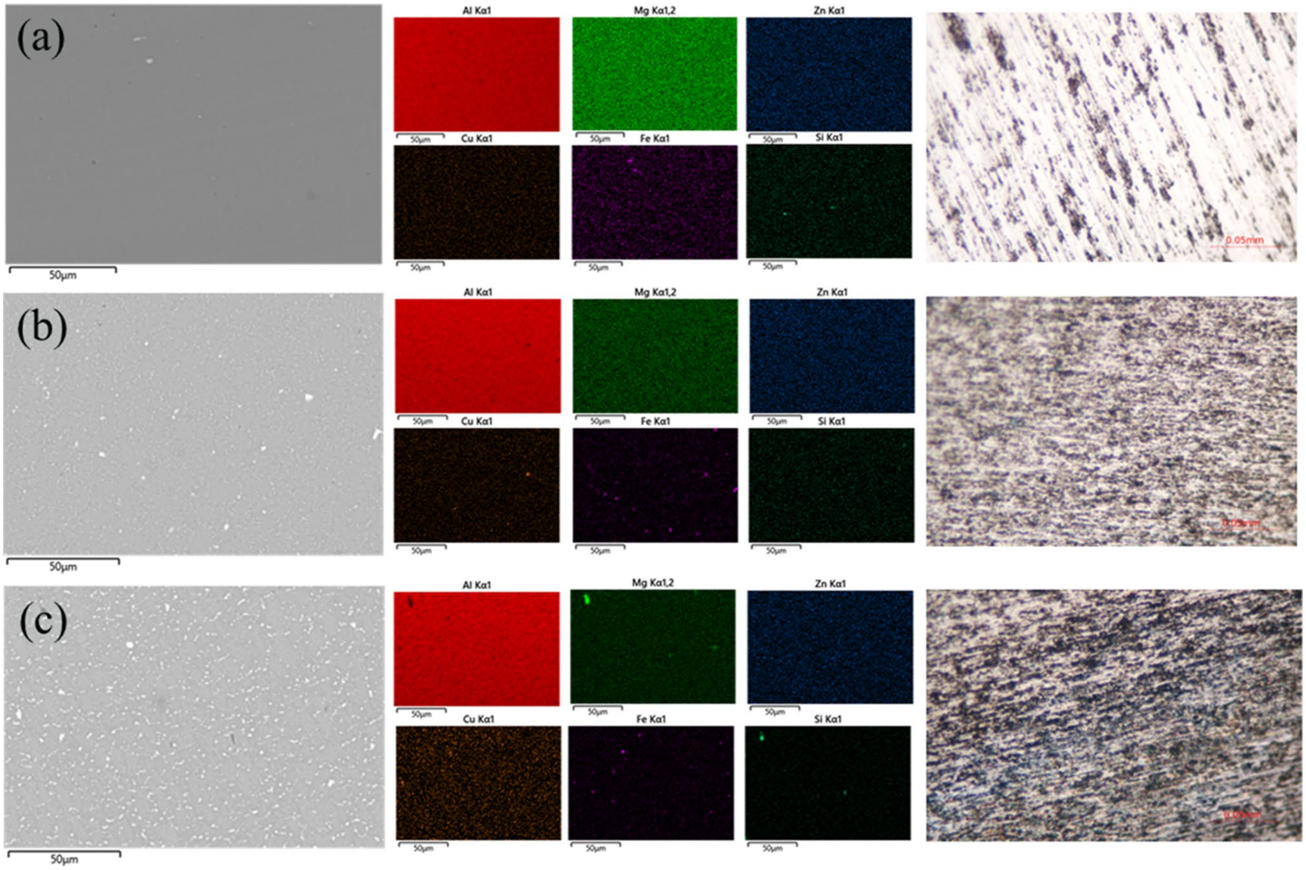

Fig. 5 BSE images, EDS mapping, and optical images of **a** feedstock, **b** as-deposited top layers, and **c** as-deposited bottom layers specimens

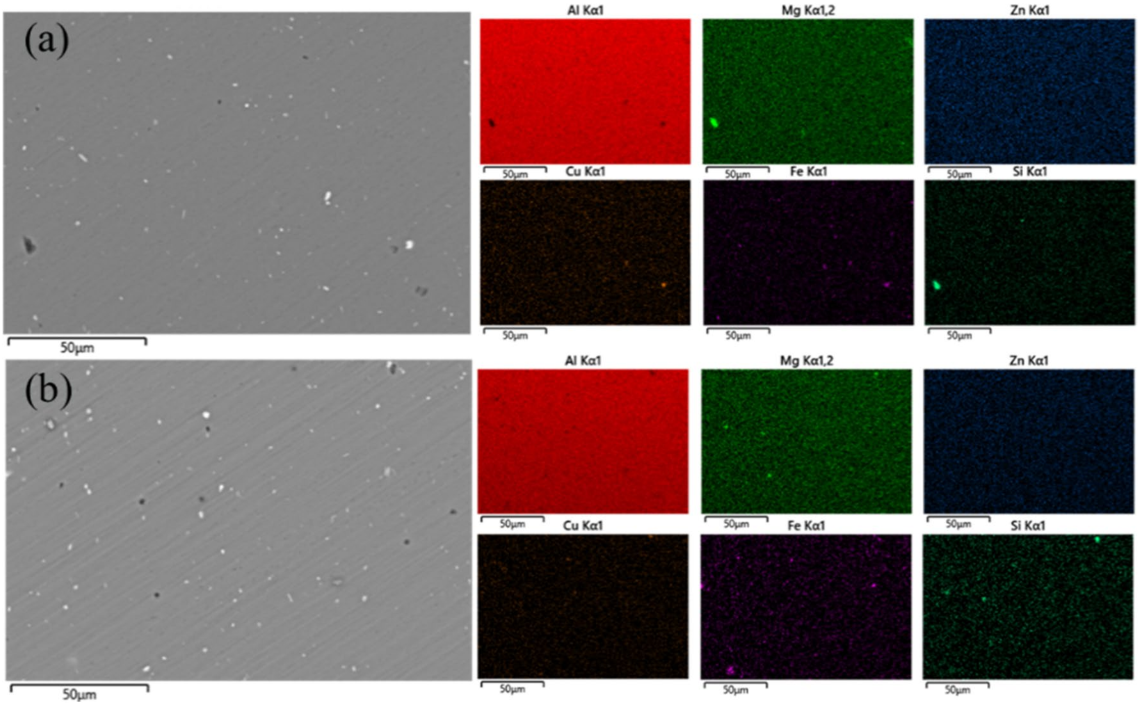

Fig. 6 BSE images and EDS mapping of heat-treated **a** top layers and **b** bottom layers specimens

Fig. 7 EBSD maps of **a** as-deposited and **b** heat-treated specimens

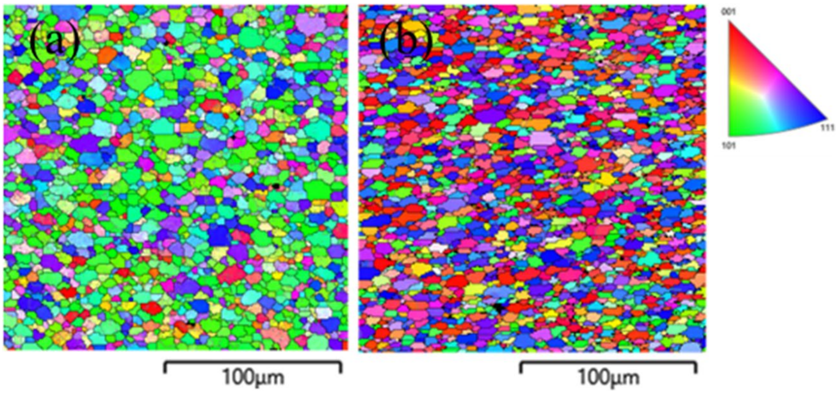

3.4 Hardness and electroconductivity measurements

Microhardness and electroconductivity tests were carried out along the cross-section center line from the top to the bottom layers (Z direction), and the results are indicated in Fig. 8. For the as-deposited part, the hardness decreased from 84.4 HV for the second layer from the top ($Z = 2.25$ mm) to 76.1 HV for the bottom layer ($Z = 38.25$ mm). The average hardness along the center line was 80.5 HV, indicating a 54.4% decrease compared to the feedstock hardness (176.5 HV). In contrast, the conductivity exhibited an opposite trend and increased from 38.7 to 40.6%IACS for the mentioned layers. Additionally, the average conductivity of the as-deposited cross-section enhanced from 33.3 to 39.8%IACS in comparison to the feedstock material. These changes in the properties could be justified by the microstructure results. For a precipitation-hardened alloy such as Al 7075, the secondary phases in the matrix develop distortions in the crystal lattice structure of the material due to their composition and structure difference. These lattice distortions act as barriers to the dislocation movement and make the alloy harder. On the other hand, the precipitations and distortions scatter free electrons in the material and deteriorate the electrical conductivity [38, 39]. For the as-deposited part of this study, large and aggregated precipitations were observed in the microstructure which were less effective in hindering the dislocation movement. Therefore, the hardness

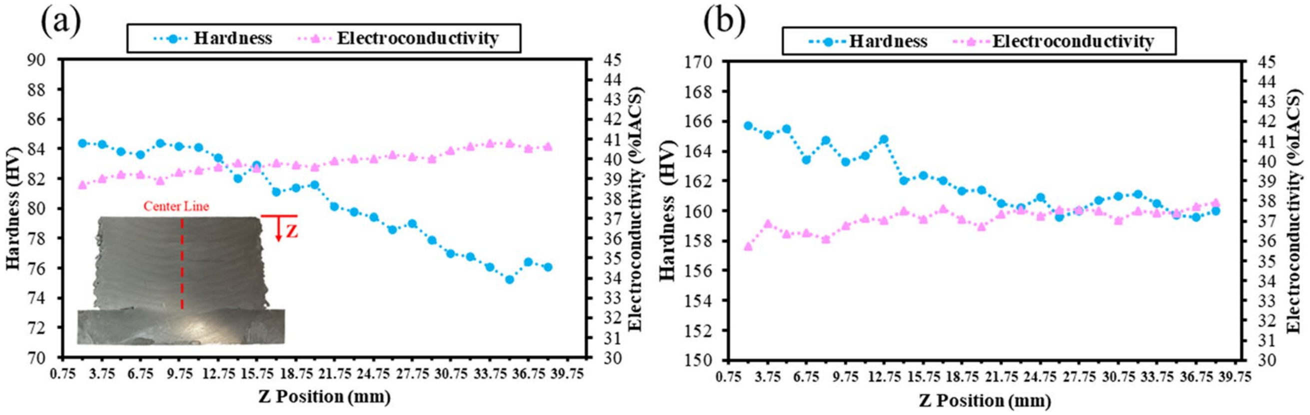

Fig. 8 Electroconductivity and hardness data along the cross-section center line for **a** as-deposited and **b** heat-treated specimens

was significantly reduced compared to the feedstock. The reduction in the hardness from the top to the bottom layers could be ascribed to the coarsening of the precipitation in the bottom layers due to experiencing more heating cycles. Moreover, the conductivity of the AFSD specimen increased due to the reduction in the overall lattice distortions and the scattering effect. The electrons could move more freely in the bottom layers due to the precipitation coarsening in these layers. The average hardness significantly enhanced to 162.0 HV, and the electroconductivity changed to 37.1%IACS after the heat treatment. Furthermore, the change in the properties from the top to the bottom layers became less significant. A hardness of 165.7 HV was measured for the second top layer which decreased to 160.0 HV for the bottom layer. The conductivity improved from 35.7 to 37.9%IACS for the mentioned layers. The considerable enhancement in the hardness and the decrease in the electroconductivity could be attributed to the change in the size and distribution of secondary phases after the heat treatment which impedes the dislocation movement and increases electron scattering. Similar results were reported for the hardness and electroconductivity of Al 7075 after heat treatment [38, 40].

3.5 Tensile properties

Figure 9 illustrates the strain–stress curves obtained from tensile testing of the specimens in the longitudinal direction before and after the heat treatment, and the results are summarized in Fig. 10. According to the supplier, the ultimate stress and elongation at break for the Al 7075-T651 feedstock material were 551.6 MPa and 8.2%, respectively. The ultimate stress of the as-deposited parts decreased to 311.7 and 287.6 MPa for the top and bottom layers, respectively. However, the ductility enhanced; the elongation at break increased to 17.8 and 21.9% for the corresponding layers. The significant decrease in the strength and the ductility enhancement for the as-fabricated AFSD parts were related to the increased dislocation movements because of the

Fig. 9 Stress–strain curves for the as-deposited and heat-treated specimens

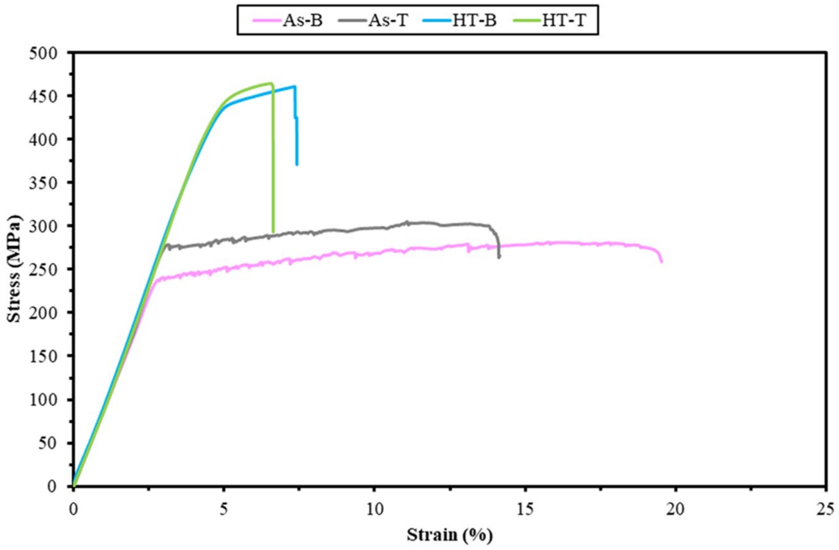

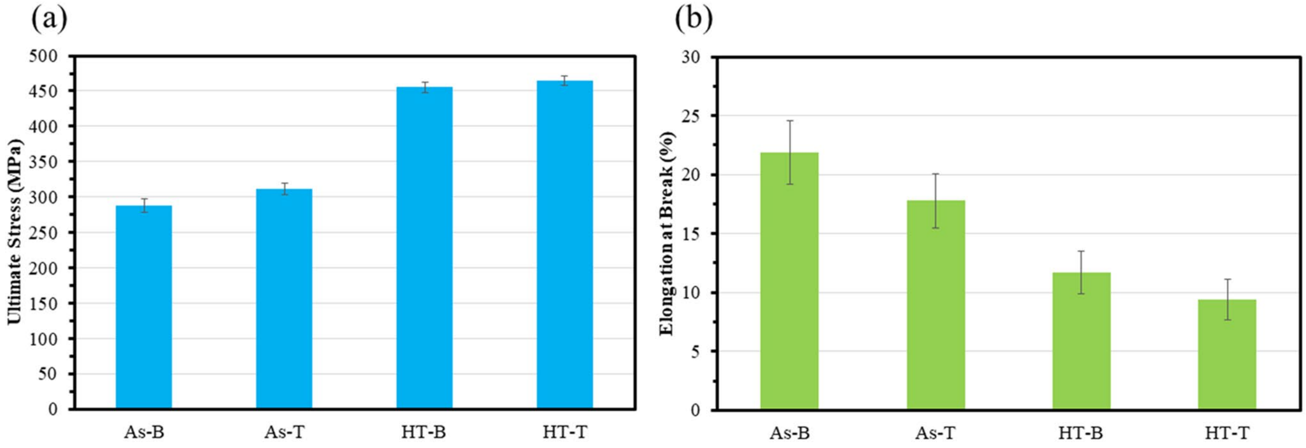

Fig. 10 Ultimate strength and elongation at break for the samples before and after heat treatment

non-uniform distribution and aggregation of precipitations after the process. However, the ultimate strength improved to about 464.9 MPa and the elongation decreased to approximately 9.4% after the heat treatment, suggesting that smaller precipitates were formed uniformly [41]. The dislocation pinning effect by the fine precipitates makes the material less capable of undergoing large deformations before fracture, reducing the ductility. The results are in good agreement with the hardness measurements and the microstructure data.

4 Conclusions

In the present work, the processing parameters for 3D printing Al 7075 parts by AFSD were first discussed in detail. Next, the microstructure, electroconductivity, and mechanical properties of the deposited parts were studied. The results revealed that the average hardness and electroconductivity of the as-fabricated Al7075 blocks were 80.5 HV and 39.8%IACS, much different from the feedstock material values of 175.5 HV and 33.3%IACS. In addition, the tensile strength decreased from 551.6 to 311.7 MPa. Heat treatment was carried out successfully for the purpose of properties recovery. The hardness and strength were improved to 162 HV and 464.9 MPa, respectively, and the conductivity decreased to 37.1%IACS. The microstructure analysis revealed that the changes in the size and distribution of the precipitations in the matrix after the process were the reason for the shifts in the properties.

Author contribution Ehsan Bagheri contributed to the study conception and design, material preparation, data collection, and analysis. Saeid Zavari, Noushin Adibi, Huan Ding, and Hamed Ghadimi also contributed to material preparation and data collection. The original draft of the manuscript was written by Ehsan Bagheri. Shengmin Guo supervised the research and reviewed the manuscript. All authors read and approved the final manuscript.

Funding This work was supported by the US National Science Foundation under grant number OIA-1946231 and the Louisiana Board of Regents for the Louisiana Materials Design Alliance (LAMDA). SG is also partially supported by the Center for Innovations in Structural Integrity Assurance (CISIA), a National Science Foundation (NSF) Industry/University Cooperative Research Center (Award number 2052810).

Declarations

Competing interests The authors declare no competing interests.

References

1. Kushwaha AK, Rahman MH, Slateret E et al (2022) 1 - Powder bed fusion–based additive manufacturing: SLS, SLM, SHS, and DMLS. In: Kumar P, Misra M, Menezes PL (eds) Tribology of Additively Manufactured Materials. Elsevier, pp 1–37
2. Vafadar A, Guzzomi F, Rassau A, Hayward K (2021) Advances in metal additive manufacturing: a review of common processes, industrial applications, and current challenges. Appl Sci 11:1213
3. Yang T, Jin Y, Wang T, Dowden S, Neogi A, Dahotre NB (2024) Stress interference in multilayer additive friction stir deposition of AA6061 aluminum. Int J Adv Manuf Technol. https://doi.org/10.1007/s00170-024-13688-4
4. Tang W, Yang X, Tian C (2023) Influence of rotation speed on interfacial bonding mechanism and mechanical performance of aluminum 6061 fabricated by multilayer friction-based additive manufacturing. Int J Adv Manuf Technol 126:4119–4133. https://doi.org/10.1007/s00170-023-11378-1
5. Martin LP, Luccitti A, Walluk M (2022) Repair of aluminum 6061 plate by additive friction stir deposition. Int J Adv Manuf Technol 118:759–773. https://doi.org/10.1007/s00170-021-07953-z
6. Shao J, Samaei A, Xue T et al (2023) Additive friction stir deposition of metallic materials: process, structure and properties. Mater Des 234:112356. https://doi.org/10.1016/j.matdes.2023.112356
7. Mukhopadhyay A, Saha P (2022) A critical review on process metrics–microstructural evolution–process performance correlation in

additive friction stir deposition (AFS-D). J Braz Soc Mech Sci Eng 44:422. https://doi.org/10.1007/s40430-022-03729-y
8. Ahmed MMZ, El-Sayed Seleman MM, Elfishawy E, Alzahrani B, Touileb K, Habba MIA (2021) The effect of temper condition and feeding speed on the additive manufacturing of AA2011 parts using friction stir deposition. Materials 14:6396
9. Avery DZ, Phillips BJ, Mason CJT (2020) Influence of grain refinement and microstructure on fatigue behavior for solid-state additively manufactured Al-Zn-Mg-Cu alloy. Metall Mater Trans A 51:2778–2795. https://doi.org/10.1007/s11661-020-05746-9
10. Cahalan LP, Williams MB, Brewer LN (2024) Parametric investigation of parallel deposition passes on the microstructure and mechanical properties of 7075 aluminum alloy processed with additive friction stir deposition. Appl Sci 14:457
11. Chen G, Wu K, Wang Y et al (2023) Quantitative study on the correlation between microstructure and mechanical properties of additive friction stir deposited 6061–T6 Al-Mg-Si alloy. J Mater Res Technol 25:6725–6736. https://doi.org/10.1016/j.jmrt.2023.07.097
12. Chen L, Zhu L, Lu L, Yang Z, Ren X, Zhang X (2024) The effect of heat treatment on the microstructure and electrochemical corrosion behavior of multilayer AA6061 alloy fabricated by additive friction stir deposition. Appl Surf Sci 650:159167. https://doi.org/10.1016/j.apsusc.2023.159167
13. Elshaghoul YGY, El-Sayed Seleman MM, Bakkar A et al (2023) (2023) Additive friction stir deposition of AA7075-T6 alloy: impact of process parameters on the microstructures and properties of the continuously deposited multilayered parts. Appl Sci 13:10255
14. Ghadimi G, Ding H, Emanet S et al (2023) Hardness distribution of Al2050 parts fabricated using additive friction stir deposition. Materials 16:1278
15. Ghadimi H, Talachian M, Ding H, Emanet S, Guo S (2024) The effects of layer thickness on the mechanical properties of additive friction stir deposition-fabricated aluminum alloy 6061 parts. Metal 14:101
16. Hu F, Chen G, Lin Y, Wang H, Zhu Z (2024) Numerical and experimental study on the thermal process during additive friction stir deposition. CIRP J Manuf Sci Technol 48:55–66. https://doi.org/10.1016/j.cirpj.2023.12.002
17. Jin Y, Wang T, Liu T et al (2024) Gradient process parameter optimization in additive friction stir deposition of aluminum alloys. Int J Mach Tools Manuf 195:104113. https://doi.org/10.1016/j.ijmachtools.2023.104113
18. Li Y, Yang B, Zhang M et al (2023) The corrosion behavior and mechanical properties of 5083 Al-Mg alloy manufactured by additive friction stir deposition. Corros Sci 213:110972. https://doi.org/10.1016/j.corsci.2023.110972
19. Li Y, Zhang M, Wang H, Lai R, Yang B, Li Y (2023) Microstructure and mechanical properties of Al–Li alloy manufactured by additive friction stir deposition. Mater Sci Eng: A 887:145753. https://doi.org/10.1016/j.msea.2023.1457534
20. Mason CJT, Rodriguez RI, Avery DZ et al (2021) Process-structure-property relations for as-deposited solid-state additively manufactured high-strength aluminum alloy. Addit Manuf 40:101879. https://doi.org/10.1016/j.addma.2021.101879
21. Metz PC, Franz C, Kincaid J et al (2024) Heterogeneous microstructure development in additive friction-stir deposited Al-Mg-Si alloy. Addit Manuf 81:103989. https://doi.org/10.1016/j.addma.2024.103989
22. Phillips BJ, Williamson CJ, Kinser RP, Jordon JB, Doherty KJ, Allison PG (2021) Microstructural and mechanical characterization of additive friction stir-deposition of aluminum alloy 5083 effect of lubrication on material anisotropy. Materials 14:6732
23. Rivera OG, Allison PG, Brewer LN et al (2018) Influence of texture and grain refinement on the mechanical behavior of AA2219 fabricated by high shear solid state material deposition. Mater Sci Eng: A 724:547–558. https://doi.org/10.1016/j.msea.2018.03.088
24. Zeng C, Ghadimi H, Ding H et al (2022) Microstructure evolution of Al6061 alloy made by additive friction stir deposition. Materials 15:3676
25. Zhang Y, Guan X, Wang L, Wang X, Zhan X (2023) The microstructure diversity in different areas of the ring-route Al 6061–T6 additive zone by friction stir additive manufacturing. Int J Adv Manuf Technol 128:4857–4871. https://doi.org/10.1007/s00170-023-11882-4
26. Yu HZ, Hahn GD (2023) Potential and challenges for large-scale near-net-shaping of 7xxx aerospace grade aluminum via additive friction stir deposition. Mater Lett: X 19:100217. https://doi.org/10.1016/j.mlblux.2023.100217
27. Griffiths RJ, Petersen DT, Garcia D, Yu HZ (2019) Additive friction stir-enabled solid-state additive manufacturing for the repair of 7075 aluminum alloy. Appl Sci 9:3486
28. Stubblefield GG, Williams MB, Munther M et al (2023) Ballistic evaluation of aluminum alloy (AA) 7075 plate repaired by additive friction stir deposition using AA7075 feedstock. J Dyn Behav Mater 9:79–89. https://doi.org/10.1007/s40870-022-00363-6
29. Gotawala N, Yu HZ (2023) Material flow path and extreme thermomechanical processing history during additive friction stir deposition. J Manuf Process 101:114–127. https://doi.org/10.1016/j.jmapro.2023.05.095
30. Ansari MA, Samanta A, Behnagh RA, Ding H (2019) An efficient coupled Eulerian-Lagrangian finite element model for friction stir processing. Int J Adv Manuf Technol 101:1495–1508. https://doi.org/10.1007/s00170-018-3000-z
31. Pew JW, Nelson TW, Sorensen CD (2007) Torque based weld power model for friction stir welding. Sci Technol Weld Join 12:341–347. https://doi.org/10.1179/174329307X197601
32. Funazuka T, Dohda K, Takatsuji N, Takano K, Sukunthakan N (2022) Effect of temperature on surface cracking defects in AA7075 hot extrusion. Key Eng Mater 926:409–415. https://doi.org/10.4028/p-6bfd8v
33. Wang T, Atehortua JE, Song M et al (2022) Extrusion of unhomogenized castings of 7075 aluminum via ShAPE. Mater Des 213:110374. https://doi.org/10.1016/j.matdes.2021.110374
34. Agrawal P, Haridas RS, Yadav S, Thapliyal S, Dhal A, Mishra RS et al (2023) Additive friction stir deposition of SS316: effect of process parameters on microstructure evolution. Mater Charact 195:112470. https://doi.org/10.1016/j.matchar.2022.112470
35. Bayazid SM, Farhangi H, Asgharzadeh H, Radan L, Ghahramani A, Mirhaji A (2016) Effect of cyclic solution treatment on microstructure and mechanical properties of friction stir welded 7075 Al alloy. Mater Sci Eng A 649:293–300
36. Li G, Jadhav SD, Martín A, Montero-Sistiaga ML et al (2021) Investigation of solidification and precipitation behavior of Si-modified 7075 aluminum alloy fabricated by laser-based powder bed fusion. Metall Mater Trans A 52:194–210. https://doi.org/10.1007/s11661-020-06073-9
37. Girish G (2023) Effect of tool pin geometry and multi-pass intermittent friction stir processing on the surface properties of aerospace grade aluminium 7075 alloy. Proc Inst Mech Eng, Part E: J Process Mech Eng 09544089231158948. https://doi.org/10.1177/09544089231158948
38. Pankade SB, Khedekar DS, Gogte CL (2018) The influence of heat treatments on electrical conductivity and corrosion performance of AA 7075–T6 aluminium alloy. Procedia Manuf 20:53–58. https://doi.org/10.1016/j.promfg.2018.02.007
39. Şimşek I (2019) Investigation of the effect of second phase precipitates on the corrosion and electrical conductivity of 7075 aluminum alloys. Anti-corros Method M 66:683–688. https://doi.org/10.1108/ACMM-02-2019-2082

40. James S, Roy A (2020) Study of aging heat treatment parameters for 7050 and 7075 aluminum alloys, ASME 2020 15th International Manufacturing Science and Engineering Conference Volume 2: Manufacturing Processes; Manufacturing Systems; Nano/Micro/Meso Manufacturing; Quality and Reliability. https://doi.org/10.1115/MSEC2020-8348
41. Rokni MR, Widener CA, Champagne VK, Crawford GA, Nutt SR (2017) The effects of heat treatment on 7075 Al cold spray deposits. Surf Coat Technol 310:278–285. https://doi.org/10.1016/j.surfcoat.2016.10.064